

# Multi-scale Design and Synthesis Strategy of Ni-doped SnO<sub>2</sub> Hollow Spheres as Anode Material for Lithium-ion Batteries

Peng Ou<sup>1,2</sup>, Zengqiang Cao<sup>1,\*</sup>, Ju Rong<sup>3,\*</sup>

<sup>1</sup> School of Mechanical Engineering, Northwestern Polytechnical University, 127 Youyi ave, West, Xi'an 710072, China

<sup>2</sup> Kunming Precision Machinery Research Institute, PO Box No.26, Kunming 650118, China

<sup>3</sup> Faculty of Materials Science and Engineering, Kunming University of Science and Technology, Kunming 650093, China

\*E-mail: [2018100130@mail.nwpu.edu.cn](mailto:2018100130@mail.nwpu.edu.cn), [cjq66326@mail.nwpu.edu.cn](mailto:cjq66326@mail.nwpu.edu.cn), [JRong\\_kmust@163.com](mailto:JRong_kmust@163.com)

Received: 4 March 2022 / Accepted: 20 April 2022 / Published: 6 June 2022

The rational design and synthesis of electrode materials with tailored structures is especially attractive for energy storage and conversion. Herein, we develop a new point-to-point on-demand designed and synthesized strategy to overcome SnO<sub>2</sub> anode material suffers from the low ion/electron conductivity and huge volume change (~300%) problems. We demonstrate that Ni-doped SnO<sub>2</sub> hollow spheres multilevel structure exhibit high reversible capacity and excellent cycle stability: the initial specific discharge capacity is up to 1581 mAhg<sup>-1</sup> and the reversible capacity remains 542 mAhg<sup>-1</sup> after 300 cycles, which is much higher than that of the commercial graphite (372 mAhg<sup>-1</sup>). These satisfactory electrochemical properties are mainly attributed to unique structure of Ni-doped SnO<sub>2</sub> hollow spheres in which Ni-doped SnO<sub>2</sub> leads to good electron transfer efficiency and structural stability, the nanostructure can effectively reduce the lithium ion diffusion activation energy and band gap width, moreover hollow spheres structure is able to improve the comprehensive transmission efficiency and avoid pulverization associated with volume changes. This work provides new insights into the practical use of SnO<sub>2</sub> anode material for lithium-ion batteries.

**Keywords:** Doping engineering; SnO<sub>2</sub> hollow sphere; lithium-ion batteries; multi-scale structure; volume change

## 1. INTRODUCTION

The design and synthesis of electrode materials with high electrochemical performance, especially high reversible capacity and excellent cycle stability, are critical to respond to the increasing demand for portable electronic devices and electric vehicles [1,2]. Among the available anode materials,

tin oxide ( $\text{SnO}_2$ )-based materials are particularly promising candidates due to their high theoretical capacity ( $1494 \text{ mAg}^{-1}$ ), safe lithiation potential, natural abundance, low cost and environmental friendliness [3-5]. However, the large volume expansion ( $>300\%$ ) and agglomeration of  $\text{SnO}_2$  inevitably occur during the conversion reaction process, which can result in severe pulverization and large capacity fading [6,7]. Furthermore, the poor ionic and electronic conductivity of  $\text{SnO}_2$  must also be urgently solved [8,9], because  $\text{SnO}_2$ -based materials applied in Li-ion batteries are seriously limited by poor electronic conductivity.

In order to address these limitations, two applied strategies can be utilized [10]. The first approach is the rational use of nanostructured electrode materials; for instance, the development of various nanowire, nanotube, nanoneedle and hollow structures [11-13]. The second promising approach is hybridization with carbonaceous or metallic materials, which can effectively increase the ionic/electronic conductivity and avoid the pulverization associated with volume changes [14,15]. Although these two strategies provide an important basis and reference for  $\text{SnO}_2$ -based anode materials, they are still not entirely satisfactory [9]. For example, it remains challenging to rationally design nanostructures based on nanophysics and nanochemistry and high carbon contents reduce the theoretical specific capacity of electrode materials [16,17]. Therefore, the design and synthesis of  $\text{SnO}_2$  electrode materials with rational multilevel structures is a very difficult problem [18-20].

To date, some synthesis strategies for multilevel structures have been considered. Yu et al. [21] confirmed that  $\text{SnO}_2$  hollow spheres with a thickness of 15 nm greatly improved the structural stability of the anode material, increased the specific surface areas between the electrode and electrolyte and simultaneously shortened the transport distances between electrons and Li ions. Yang et al. [22] found that the Li-ion storage capacity and electronic conductivity of  $\text{SnO}_2$  electrodes could be improved by a three-dimensional graphene-caged carbon hybridized structure, which retained a reversible capacity of  $474 \text{ mAg}^{-1}$  after 300 cycles. Aragon et al. [23] showed the effect of Ni doping on the volume expansion and electronic conductivity of  $\text{SnO}_2$  nanoparticles and reported that the crystallite size and electronic conductivity decreased with increasing Ni content, while the unit cell volume and residual strain did not show any clear dependence. The above research illustrated that synthesis strategies for multilevel  $\text{SnO}_2$  nanomaterials were essential for obtaining high battery performance.

Unfortunately, it remains a challenge to integrate and design the variation regularity of the volume expansion and ionic and electronic conductivity of  $\text{SnO}_2$  by first principles, nanothermodynamics and nanodynamics. This is because the specific relationship between the electrochemical performance, nanostructure, grain size and doping content remains unclear. Furthermore, the integrated design ideas achieved experimentally are too difficult to carry out. Consequently, the development of a new point-to-point on-demand design and synthesis strategy to overcome the challenges in the synthesis process of multilevel structures is necessary.

Here, we developed an ingenious strategy to synthesize Ni-doped  $\text{SnO}_2$  hollow spheres with a multilevel structure by first principles and nanothermodynamic calculations. Considering the electronic conductivity, volume expansion and diffusion transport energy of  $\text{SnO}_2$ , the atomic radii of the transition metal dopants should be close to the Sn ions, while first principles simulations and previous reports strongly suggested that Ni should be considered [23]. In addition, the band gap and Li-ion diffusion activation energy were affected by the cohesive energy and size, and our nanothermodynamic model

showed that a thickness of ~20 nm displayed good electronic conductivity and ionic electrons for metal oxides [24-26]. More importantly, the methods for reducing volume expansion should include hollow spheres, which can improve the comprehensive transmission efficiency and avoid the pulverization associated with volume changes [9]. As a simple example of multiscale design, our Ni-doped SnO<sub>2</sub> hollow spheres exhibited a high reversible capacity and excellent cycle stability that was much higher than that of commercial graphite. Consequently, our work provides guidance to improve the electrochemical performance of nanomaterials by controlling their multilevel structure.

## 2. EXPERIMENT SECTION

### 2.1 Synthesis of SiO<sub>2</sub> spheres

SnO<sub>2</sub> spheres were synthesized via the Stober method [27]. Specifically, 100 mL of ethanol and 15 mL of 28% ammonia were mixed evenly by magnetic stirring for 30 min at room temperature. Then, 7.5 mL of tetraethyl orthosilicate were added dropwise and maintained under mild magnetic stirring for 10 h. After centrifugation, washing and drying, the SnO<sub>2</sub> spheres were obtained.

### 2.2 Synthesis of Ni-doped SnO<sub>2</sub> hollow spheres

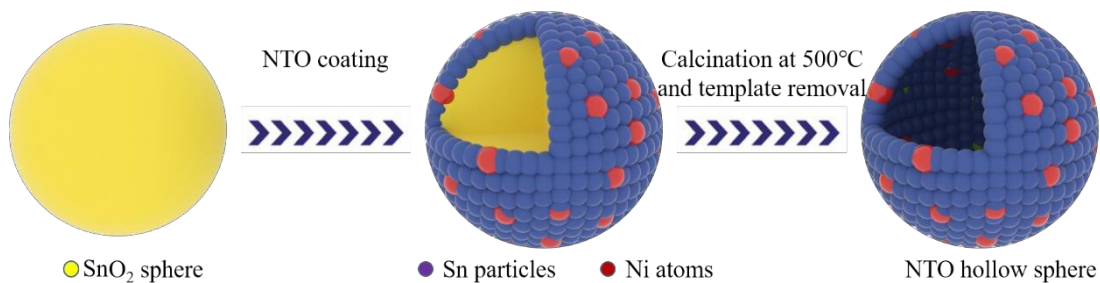


**Figure 1.** Schematic illustration of the formation process of Ni-doped SnO<sub>2</sub> hollow spheres.

Ni-doped SnO<sub>2</sub> hollow spheres were prepared using a hydrothermal reaction, as schematically depicted in Figure 1. First, 0.13 g of sodium stannate ( $\text{Na}_2\text{SnO}_3 \cdot 3\text{H}_2\text{O}$ ), 0.9 g of urea and a certain amount of nickel nitrate hexahydrate ( $\text{NiNO}_3 \cdot 6\text{H}_2\text{O}$ ) were dissolved in 9 mL of ethanol and 15 mL of a deionized water mixed solution. After stirring for 30 min at room temperature, 0.12 g of SnO<sub>2</sub> spheres were added to the mixed solution, followed by ultrasonication for 30 min. Afterwards, the white suspension produced was poured into a reactor and heated at 170 °C for 36 h. Finally, the centrifuged and washed materials were etched with 20% hydrofluoric acid and annealed at 500°C for 4 h under argon protection to obtain the Ni-doped SnO<sub>2</sub> hollow spheres. The synthesized samples were named as NTO-0, NTO-1, NTO-2 and NTO-3, corresponding to their Ni:Sn molar ratios of 0:1, 0:2.5, 1:5 and 1:10, respectively.

### 2.3 Sample characterization

Scanning electron microscopy (SEM, TESCAN VEGA3), field emission scanning electron microscopy (FESEM, FEI Nova NanoSEM450) was used to investigate the low magnification morphology. The morphologies of the Ni-doped SnO<sub>2</sub> hollow spheres were characterized by high resolution transmission electron microscopy (HRTEM, Tecnai G2 20 S-TWIN). Their elemental distribution was analyzed by X-ray energy dispersive spectroscopy (EDS). X-ray diffraction (XRD, D/MAX-2200), using Cu-K $\alpha$  as the X-ray source, was carried out to investigate the phase structures. The valence states of the surface elements were obtained by X-ray photoelectron spectroscopy (XPS, PHI 5000).

### 2.4 Electrochemical measurements

In order to test the electrochemical performance, CR2025 coin cells were assembled in an Ar-filled glove box. A lithium sheet and the Ni-doped SnO<sub>2</sub> hollow spheres acted as the cathode and anode, respectively. A composite membrane of porous polyethylene/polypropylene (Celgard-2300) was used as the separator. Lithium hexafluorophosphate (1 mol/L) dissolved in a dimethyl carbonate, ethylene carbonate and diethyl carbonate mixture with a volume ratio of 1:1:1 was used as the electrolyte. After completing the assembly, a manual tablet press (MRX-YP180) was carried out to seal the battery. A LAND-2010 instrument was used to test the galvanostatic charge-discharge cycling. An electrochemical workstation (CH Instruments) was used to perform cyclic voltammetry (CV) and electrochemical impedance spectroscopy.

### 2.5 Calculation details

All calculations were completed using the Vienna Ab initio Simulation Package (VASP), which utilizes density functional theory [28,29]. The projector augmented wave approach [30] and the generalized gradient approximation based on the Perdew-Burke-Ernzerhof scheme were used [31]. The Brillouin zone was sampled with Monkhorst-Pack k-point meshes with a density of  $2\pi \times 0.02 \text{ \AA}^{-1}$  and the planewave cutoff energy was set to 500 eV [32]. In our calculations, the convergence criteria for the energy and force components were  $1 \times 10^{-6} \text{ eV}$  and  $1 \times 10^{-3} \text{ eV\AA}^{-1}$ , respectively. For the Ni-doped SnO<sub>2</sub> structure, a  $2 \times 2 \times 2$  supercell model was used to illustrate the doping effect (48 atoms).

## 3. RESULTS AND DISCUSSION

### 3.1 Multi-scale design method

In order to reduce the volume expansion and increase the electron concentration simultaneously, the crystal structures and electrical properties of the SnO<sub>2</sub> materials before and after Ni doping were assessed by first principles. Figure 2 displays the electronic energy band structure and crystal structure of pure (Figure 2a) and Ni-doped SnO<sub>2</sub> (Figure 2b). Compared with pure SnO<sub>2</sub>, the crystal structure and

lattice constant of Ni-doped  $\text{SnO}_2$  remained constant ( $a = b = 0.47 \text{ nm}$ ,  $c = 0.32 \text{ nm}$  and  $\alpha = \beta = \gamma = 90^\circ$ ) with increasing Ni content [33]. This result is consistent with previous experimental studies [23]. In addition, the added Ni took part in energy level hybridization with Sn, thus resulting in a band gap after doping of 0.71 eV, which was less than for pure  $\text{SnO}_2$  (1.15 eV). In other words, the amount of electrons and the probability of electron transition in  $\text{SnO}_2$  materials increased with the addition of Ni.

Due to the specific relationship between the electrochemical properties and the nanoscale still being not fully understood, it is a challenge to design high-performance electrode nanomaterials. Fortunately, our previous nanothermodynamic model [24,25] has proven that the self- and interdiffusion activation energies of alloys exhibited a size effect that was approximately inversely proportional to the nanoscale, suggesting that a suitable nanometer size could optimize the ionic conductivity (Supplementary Note 1). For example, the relationship between the self-diffusion activation energy, nanoparticle radius and vacancy formation energy of gold nanoparticles has already been proved, which might be because of the synergistic effects of dangling bonds and defects (Supplementary Note 2) [25]. Moreover, the chemical reactivity of anatase  $\text{TiO}_2$  nanotubes and  $\text{MgO}$  and  $\text{ZnO}$  nanoparticles was also verified and it was predicted that a thickness of  $\sim 20 \text{ nm}$  should display good ionic and electronic conductivity [34]. Recently, the influence of this size effect on the band structure has also been studied, with the band gap decreasing with increasing film thickness (Supplementary Note 3) [24,35]. Therefore, based on previous theoretical works, a structure with a thickness of  $\sim 20 \text{ nm}$  was carefully chosen, which can effectively improve the ionic and electronic conductivity of  $\text{SnO}_2$ .

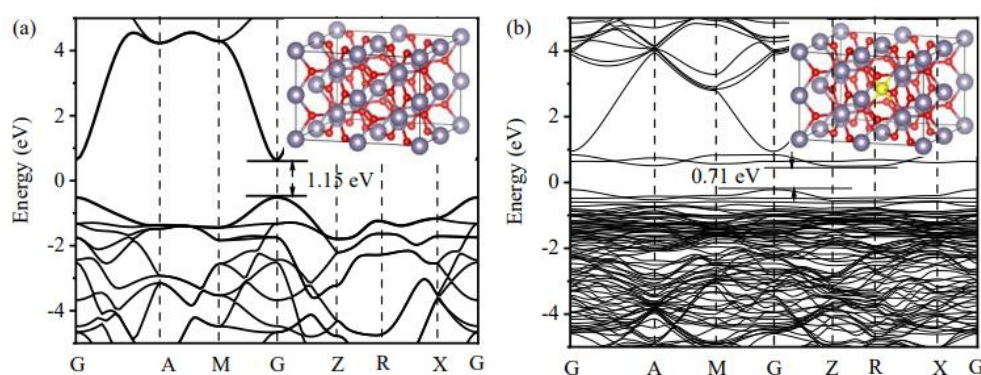


**Figure 2.** Electronic energy band structure and crystal structure of (a) pure  $\text{SnO}_2$  and (b) Ni-doped  $\text{SnO}_2$ .

In addition to doping and nanosizing, nanostructures must also be considered. In 2005, Qi et al. [36] proposed a shape-factor concept and indicated that the particle shape should be taken into consideration when calculating the surface activity. Furthermore, Kumar et al. [37] calculated the vibration and thermodynamic properties of nanostructures with different dimensions, indicating that the shape factor of a spherical nanosolid was three times that of a nanofilm. Furthermore, we found from nanothermodynamics and electrochemical experiments that hollow spheres were able to improve the comprehensive transmission efficiency and avoided the pulverization associated with volume changes (Supplementary Note 4) [9,24]. In conclusion, Ni-doped  $\text{SnO}_2$  hollow spheres may be a satisfactory

basic structure without considering coating modifications based on first principles and nanothermodynamics.

### 3.2 Structure and chemical composition of materials

The microstructures of the SnO<sub>2</sub> powder and Ni-doped SnO<sub>2</sub> hollow spheres were imaged by SEM, FESEM and EDS (Figure 3). As illustrated in Figure 3a and its inset, the SnO<sub>2</sub> powder was constructed of well-dispersed and uniformly sized nanoparticles with a diameter of ~500 nm. In addition, the SEM images of the NTO-0, NTO-1, NTO-2 and NTO-3 samples are shown in Figure 3b, displaying a hollow spherical structure.

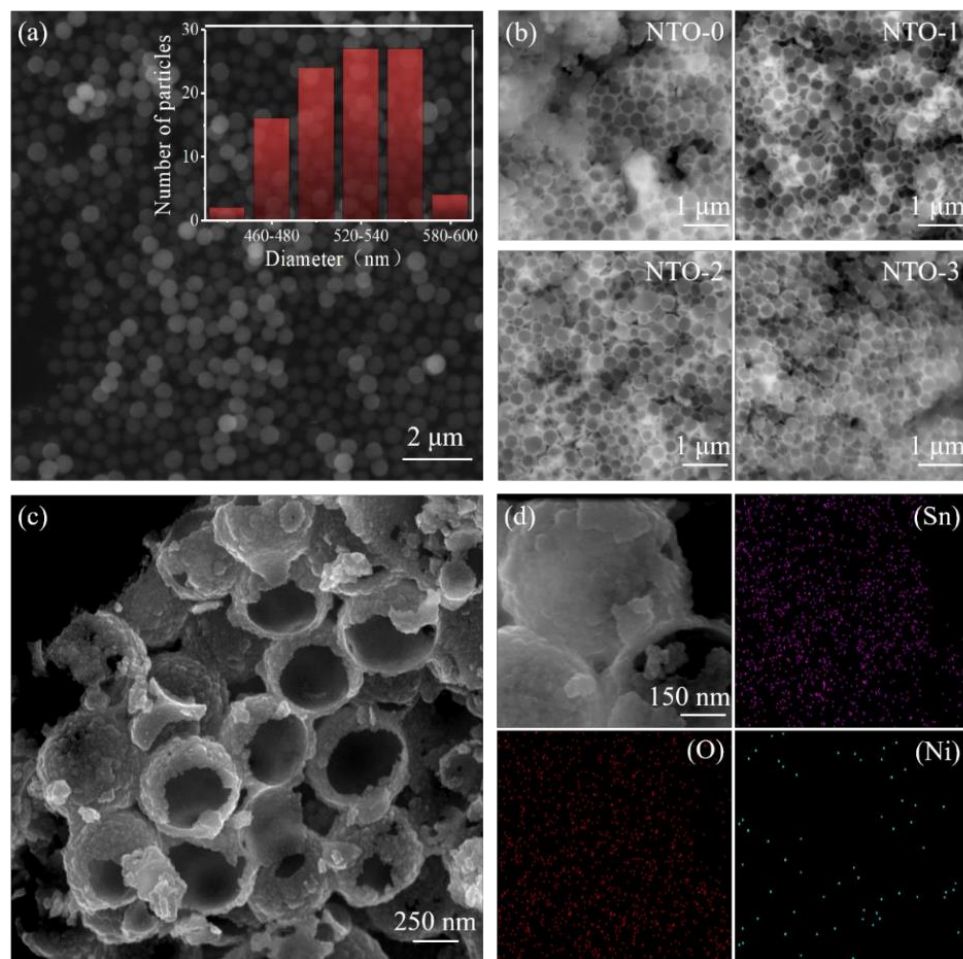


**Figure 3.** Morphology of (a) SnO<sub>2</sub> powder, (b) the NTO-0, NTO-1, NTO-2 and NTO-3 samples (c) fine microstructures of NTO-2. (d) morphology and corresponding energy-dispersive X-ray elemental mappings of NTO-2.

The samples exhibited different wall thickness due to the change in Ni doping concentration, which was of benefit for alleviating the volume expansion. Figure 3c displays the morphology and surface microstructures of NTO-2. It can be clearly seen that the wall thickness was ~20 nm and the surface presented nanostructures, indicating that this sample may have satisfactory electrochemical

activity. Moreover, Figure 3d shows the morphology and corresponding energy-dispersive X-ray elemental mappings, which proved that Sn, O and Ni were uniformly distributed in NTO-2.

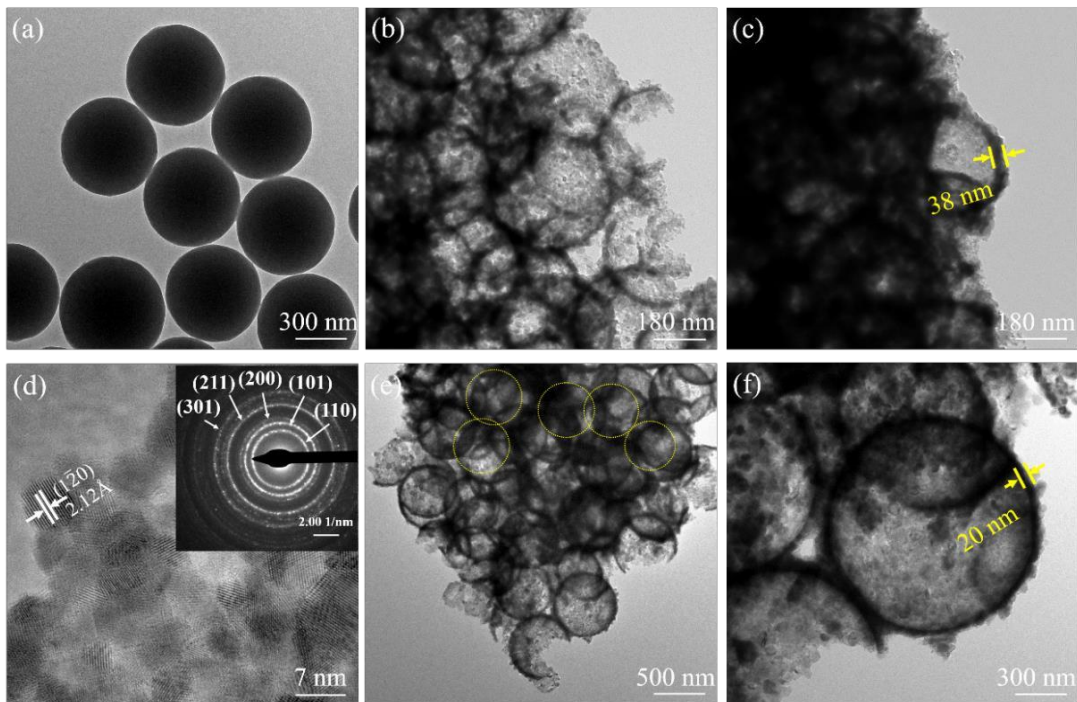
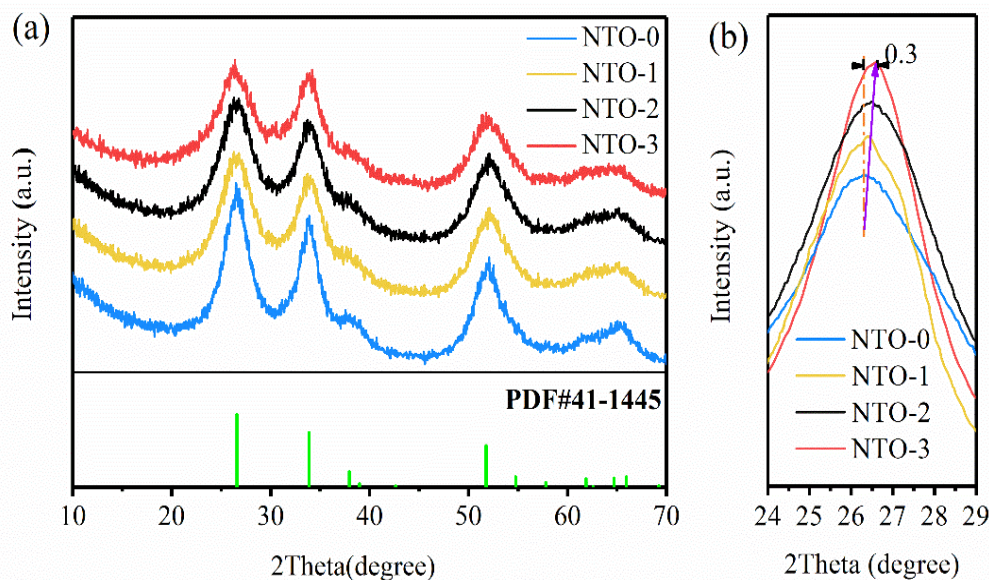


**Figure 4.** HR-TEM images of SiO<sub>2</sub> spheres (a), NTO-0 sample (b~d), and NTO-2 sample (e, f). Inset in (d) shows the corresponding SAED pattern.

TEM was used to characterize the interior microstructures of the SnO<sub>2</sub> powder and Ni-doped SnO<sub>2</sub> hollow spheres, as shown in Figure 4. The image of the SnO<sub>2</sub> powder in Figure 4a shows that the particle size was basically consistent with Figure 3. Furthermore, Figure 4d shows the selected area electron diffraction images of the crystal structure of NTO-0. As can be seen from Figure 4d, five bright diffraction rings were indexed as the (301), (211), (200), (101) and (110) planes of the rutile phase of SnO<sub>2</sub>, illustrating that the sample exhibited good crystallinity. Meanwhile, the lattice plane spacing of 0.212 nm corresponded to the (1-20) planes of rutile SnO<sub>2</sub>, implying that the crystal structure of SnO<sub>2</sub> was complete.

The images of NTO-0 and NTO-2 are given in Figures 4b and e, respectively, where a hollow sphere structure can be clearly seen. Hong et al. [38] reported that porous hollow SnO<sub>2</sub> nanospheres exhibited better cycling stability than other nanostructures, owing to the shortened diffusion pathways for electrons and Li ions and the reduced volume variation. This was also seen in the images of NTO-0 and NTO-2 (Figures 4c and f). By comparing the wall thicknesses of the two samples, we found that the wall thickness of NTO-0 was close to double of that of NTO-2 and this was because Ni doping inhibited the growth of the SnO<sub>2</sub> hollow spheres. Furthermore, several studies, including a previous investigation from our laboratories, have shown that the smaller grain size not only restrains the volume expansion

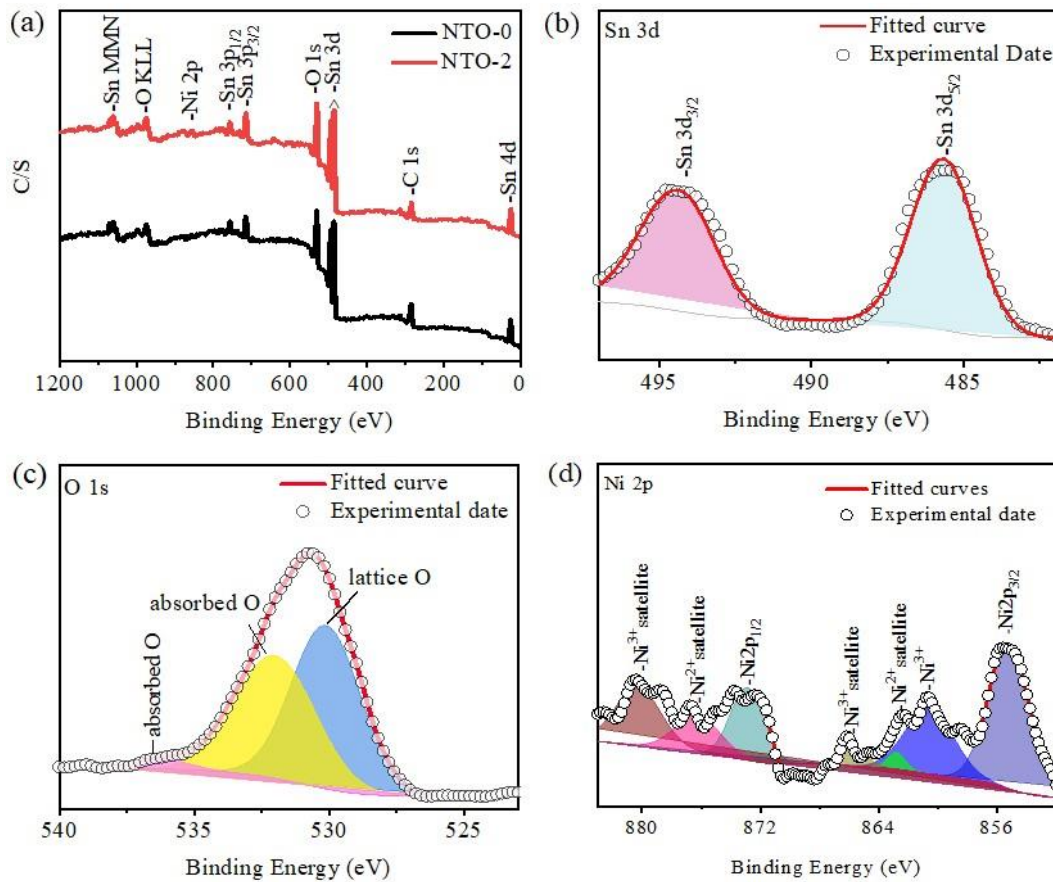
during the charge-discharge process, but also makes the wall thickness of the hollow sphere thinner, thus improving the electrochemical performance of the SnO<sub>2</sub> materials [34,39,40].



**Figure 5.** XRD patterns of Ni-doped SnO<sub>2</sub> hollow spheres: NTO-0, NTO-1, NTO-2 and NTO-3 samples (a). The magnified image of the (110) peak of the four samples (b).

An XRD analysis was utilized to characterize the crystal structures and compositions of the samples. As detailed in Figure 5a, the diffraction peaks of the SnO<sub>2</sub> materials before and after Ni doping corresponded to tetragonal rutile SnO<sub>2</sub> (JCPDS no.41-1445), confirming that the Ni atoms were incorporated into the SnO<sub>2</sub> crystal. According to the Scherrer equation ( $d = k\lambda/\beta\cos\theta$ ), the average particle sizes of NTO-0, NTO-1, NTO-2 and NTO-3 were 16.3, 12.9, 7.7 and 6.8 nm, respectively. The average particle sizes of SnO<sub>2</sub> therefore became smaller with increasing Ni content increases, in agreement with the conclusion reached from Figures 4c and f and our design theory [24,25]. This decrease strongly helped in relieving the volume expansion during the charge-discharge process. It is noteworthy that the peak at 26.7° gradually shifted towards higher angles because the ionic radius of Ni<sup>3+</sup> (0.056 nm) was smaller than that of Sn<sup>4+</sup> (0.069 nm) (see Figure 5b).

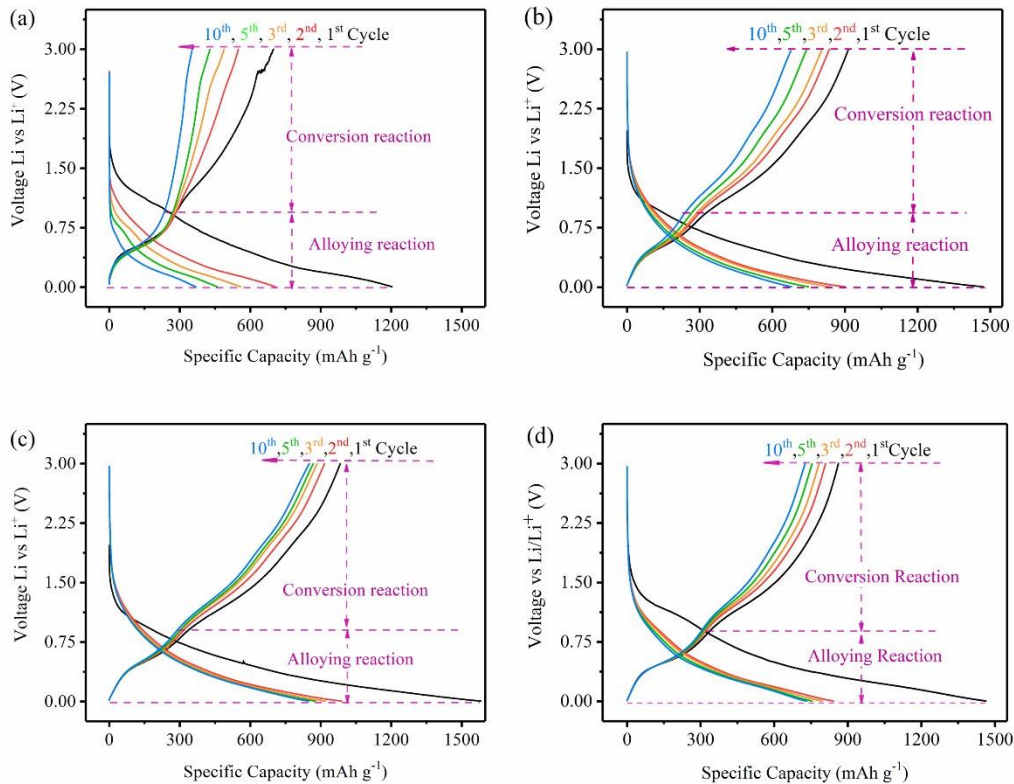
XPS characterization was conducted to reveal that the composition of NTO-1 (Figure 6a) only contained O, Sn and Ni. On this basis, we noticed that the Sn 3d peaks was decomposed into two main peaks (Figure 6b), corresponding to Sn 3d<sub>3/2</sub> and Sn 3d<sub>5/2</sub>. In addition, the O 1s peaks were also deconvoluted into two main peaks with binding energies of 531.9 and 530.2 eV, respectively (Figure 6c). The peak at 531.9 eV corresponded to the oxygen vacancies of SnO<sub>2</sub> and the peak at 530.2 eV corresponds to O<sup>2-</sup>. Notably, the Ni 2p curve could fit to two typical peaks at 860.6 and 854.9 eV, corresponding to Ni 2p<sub>3/2</sub>, while the peaks at 872.8 and 880.2 eV corresponded to Ni 2p<sub>1/2</sub> (Figure 6d) [41]. These results demonstrated that there were two main forms of Ni in the Ni-doped SnO<sub>2</sub> hollow spheres, namely, Ni<sup>2+</sup> and Ni<sup>3+</sup>.



**Figure 6.** XPS spectra of NTO-0 and NTO-2 samples: (a), survey spectrum, (b) Sn 3d, (c) O 1s, and (d) Ni 2p.

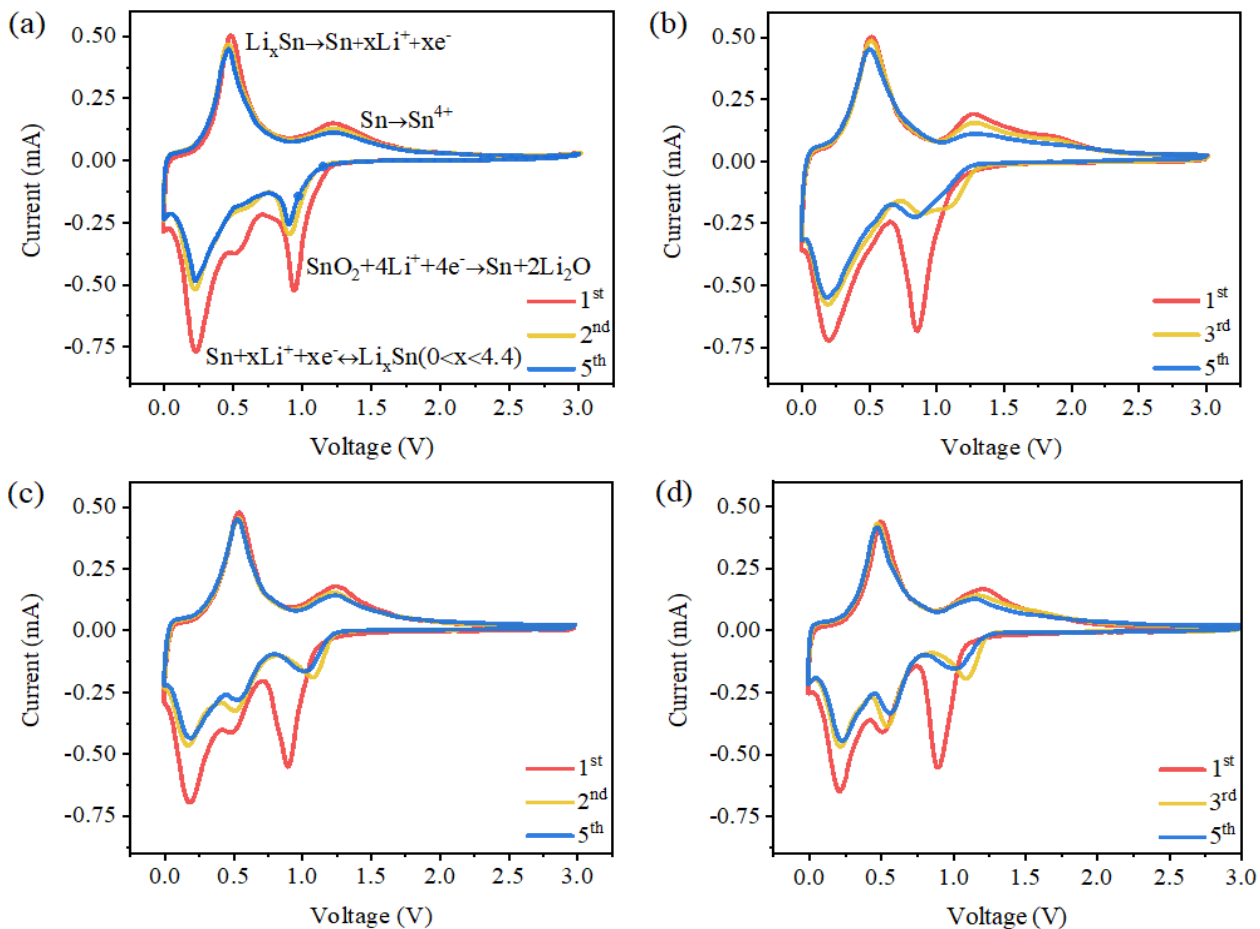
### 3.3 Electrochemical performance analysis

The electrochemical performance of the Ni-doped  $\text{SnO}_2$  hollow spheres for Li-ion batteries was also investigated. The charge-discharge properties of the first ten cycles of the samples at a current density of  $100 \text{ mA g}^{-1}$  in the voltage range of  $0.01\text{--}3 \text{ V}$  are presented in Figure 7. It can be seen that the NTO-0, NTO-1, NTO-2 and NTO-3 samples displayed initial discharge capacities of  $1203$ ,  $1470$ ,  $1581$  and  $1463 \text{ mA g}^{-1}$  and initial coulombic efficiencies of  $61.6\%$ ,  $62\%$ ,  $62.1\%$  and  $58.8\%$ , respectively. This was expected because of the decomposition of the electrolyte and the formation of a solid electrolyte interface (SEI) film on the surface of the electrode [42,43]. It is important to note that the coulomb efficiency of NTO-2 increased to almost  $100\%$  in subsequent cycles. In addition, the discharge capacities of NTO-0, NTO-1, NTO-2 and NTO-3 were  $466$ ,  $679$ ,  $851$  and  $730 \text{ mA g}^{-1}$ , respectively, which showed that the performance of the Ni-doped  $\text{SnO}_2$  electrode was better than that of the pure  $\text{SnO}_2$  electrode.



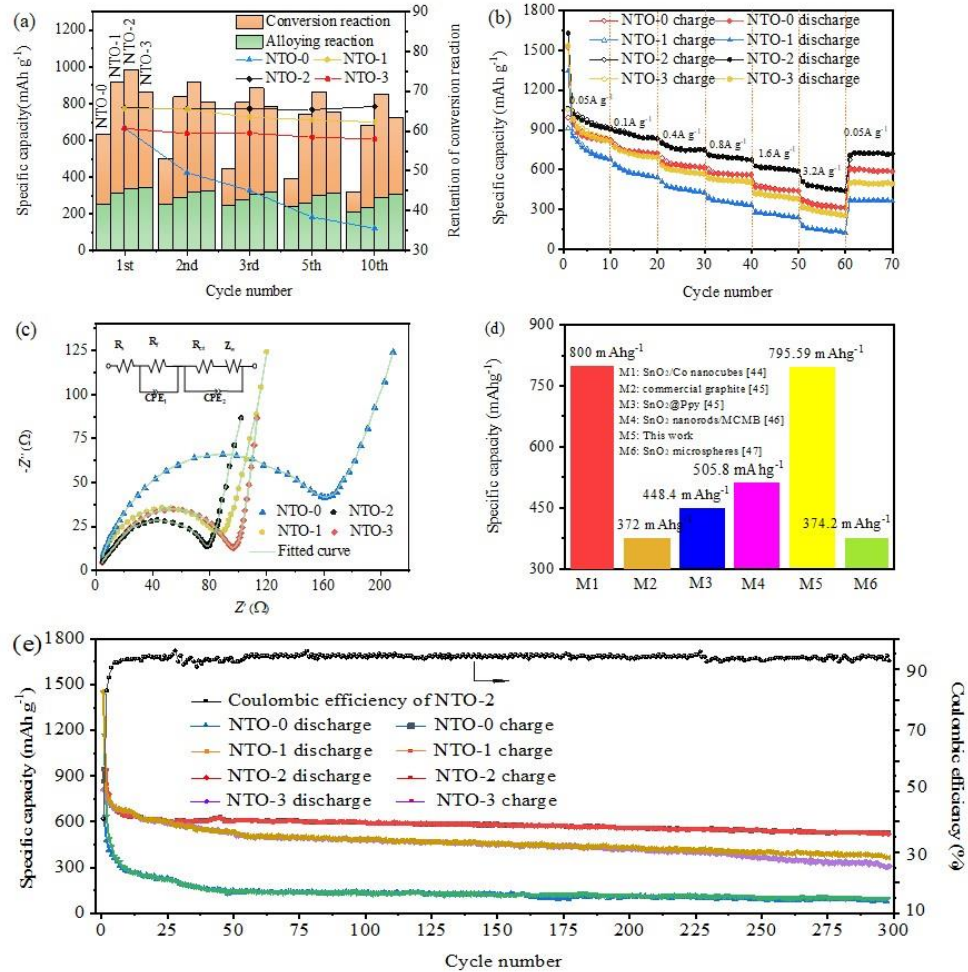
**Figure 7** The initial 10 charge-discharge curves between 0.05 V and 3 V at the current of  $100 \text{ mA} \cdot \text{g}^{-1}$  for the NTO anode electrodes: (a) NTO-0, (b) NTO-1, (c) NTO-2 and (d) NTO-3 samples.

Figure 8 presents the CV curves for the first five cycles of the NTO-0, NTO-1, NTO-2 and NTO-3 electrodes between 0.01 and -3.00 V at a scan rate of  $0.1 \text{ mVs}^{-1}$ , which are essentially consistent with the constant current charging-discharging platform. On the first cycle of NTO-0 (Figure 8a), the cathodic peak showed two components located at 0.94 and 0.23 V. The first was attributed to the formation of the SEI film on the surface of the anode, followed by the formation of  $\text{Li}_x\text{Sn}$  alloys ( $\text{Sn} + x\text{Li}^+ + xe^- \leftrightarrow \text{Li}_x\text{Sn}$  ( $0 < x < 4.4$ )) [44]. Figure 8b also shows two main anodic peaks at 0.48 and 1.24 V, which corresponded to the dealloying and oxidation processes of NTO-0, respectively. Therefore, the electrode reaction process was partially reversible. Similarly, two cathodic and anodic peaks were observed in Figures 8b-d. By comparing the CV curves of Figure 8a, the cathodic and anodic peaks were slightly shifted to 0.89, 0.18, 0.53 and 1.23 V, respectively, while the intensity of the oxidation peak was stronger than NTO-0, probably because of the Ni doping of the  $\text{SnO}_2$  hollow spheres. Moreover, the integral area of the NTO-2 electrode was also greater than NTO-0, meaning that more Li ions participated in the NTO-2 electrode reaction.



**Figure 8.** CV curve of the first five cycles between 0.01 and 3.0 V for the NTO anode electrodes: (a) NTO-0, (b) NTO-1, (c) NTO-2 and (d) NTO-3 samples.

Typically,  $\text{SnO}_2$ -based materials undergo an alloying reaction at low voltages ( $<0.85$  V) and a conversion reaction at high voltages ( $>1.25$  V). The charge-discharge specific capacity of the NTO anode materials was analyzed in Figure 9a. As can be seen, the conversion reaction of NTO-1, NTO-2 and NTO-3 was much higher than for NTO-0, with the total charge of NTO-2 up to 66.1%, while NTO-0 was only 35.5%. This result implied that Ni doping not only improved the conductive performance of the material, but also helped to improve the reversibility and cycle stability of the battery and reduce capacity attenuation.



**Figure 9.** (a) Charge capacity of NTO-0, NTO-1, NTO-2 and NTO-3 samples at the first, second, fifth and tenth cycles from the conversion and alloying reactions and the charge capacity retention of the conversion reaction at the same cycles. (b) Rate performance of NTO samples. (c) Nyquist plots of NTO samples. (d) Comparison of specific capacity of typical SnO<sub>2</sub> anode materials. (e) Cycling performance of NTO samples at a current density of 100 mA·g<sup>-1</sup>.

The charge-discharge cycle stability of the NTO electrode materials was assessed using galvanostatic charge-discharge measurements. The cycle performance curves for NTO-0, NTO-1, NTO-2 and NTO-3 at 100 mA g<sup>-1</sup> are presented in Figure 9e. It was evident that the cycle stability and specific capacity of NTO-1, NTO-2 and NTO-3 were significantly improved. These satisfactory electrochemical properties were mainly attributed to the unique structure of Ni-doped SnO<sub>2</sub> hollow spheres, which leads to good electron transfer efficiency and structural stability, as well as a reduction in the Li-ion diffusion activation energy and band gap width. Moreover, the hollow sphere structure was also able to improve the comprehensive transmission efficiency and avoid the pulverization associated with volume changes. The discharge specific capacitance of NTO-2 was maintained at 781 mAh g<sup>-1</sup> after 50 charge-discharge cycles, which was much higher than the 236 mAh g<sup>-1</sup> for NTO-0. Compared with the improvement in cycle stability, the changes in rate performance of NTO-1, NTO-2 and NTO-3 were even more obvious (Figure 9b). In particular, at a high current density of 3,200 mA g<sup>-1</sup>, NTO-2 could still deliver a reversible

capacity of  $\sim 440 \text{ mAh g}^{-1}$ , while at a current density of  $50 \text{ mA g}^{-1}$ , NTO-2 could also return to a reversible capacity of  $706 \text{ mAh g}^{-1}$ .

The relevant comparison with the cycling performance of similar anode materials is shown in Table 1 [44-48]. It was noted that the Ni-doped SnO<sub>2</sub> hollow sphere anode material exhibited good rate performance and cycling performance compared to other similar anode materials. This proved that the multiscale design was an effective method to improve the electrochemical performance of Ni-doped SnO<sub>2</sub> hollow spheres for Li-ion batteries.

**Table 1.** Comparison with cycling performance of similar anode materials

Materials	Rate performance	Cycling performance	Ref.
SnO <sub>2</sub> @TiO <sub>2</sub> nanospheres	$536 \text{ mAh g}^{-1}$ for $1000 \text{ mA g}^{-1}$	$838 \text{ mAh g}^{-1}$ for $200 \text{ mA g}^{-1}$	44
Hierarchical TiO <sub>2</sub> /SnO <sub>2</sub> hollow	$440 \text{ mAh g}^{-1}$ for $1000 \text{ mA g}^{-1}$	$644.7 \text{ mAh g}^{-1}$ for $100 \text{ mA g}^{-1}$	45
TiO <sub>2</sub> -SnO <sub>2</sub> @graphene	$388 \text{ mAh g}^{-1}$ for $1.5 \text{ A g}^{-1}$	$617 \text{ mAh g}^{-1}$ for $0.4 \text{ A g}^{-1}$	46
PAN-based carbon fiber@ SnO <sub>2</sub>	$225 \text{ mAh g}^{-1}$ for $2000 \text{ mA g}^{-1}$	$433 \text{ mAh g}^{-1}$ for $100 \text{ mA g}^{-1}$	47
3D nano-network TiO <sub>2</sub> @SnO <sub>2</sub>	$464 \text{ mAh g}^{-1}$ for $1600 \text{ mA g}^{-1}$	$836 \text{ mAh g}^{-1}$ for $200 \text{ mA g}^{-1}$	48
Ni-doped SnO <sub>2</sub> hollow spheres	$706 \text{ mAh g}^{-1}$ for $50 \text{ mA g}^{-1}$	$613 \text{ mAh g}^{-1}$ for $100 \text{ mA g}^{-1}$	This work

The electrochemical performance of the Ni-doped SnO<sub>2</sub> anodes was evaluated by alternating current impedance testing, as shown in Figure 9c. It was shown that at the high frequency region, the impedance spectra of Ni-doped SnO<sub>2</sub> were composed of a semicircle, while it was an oblique line at the low frequency region. This can be explained by the fact that at the high frequency region, the typical Nyquist semicircle represented the impedance  $R_{ct}$ , which was attributed to the charge transfer at the interface between the electrode and electrolyte. Simultaneously, the oblique line at the low frequency region was caused by the Warburg impedance  $Z_w$  of the Li-ion diffusion in the solid-phase active material [49]. It was clearly illustrated that the impedance  $R_{ct}$  and  $Z_w$  of NTO-2 were smaller than that of NTO-0, which was mainly due to the good electronic and ionic conductivity of our unique nanostructure. It can be expected that Ni-doped SnO<sub>2</sub> hollow spheres achieved satisfactory performance compared with similar materials (Figure 9d) [50-53].

#### 4. CONCLUSIONS

In summary, a new point-to-point on-demand design and synthesis strategy to overcome the low ionic/electronic conductivity and huge volume change problems associated with SnO<sub>2</sub> anodes was developed. According to the electrochemical test results, the Ni-doped SnO<sub>2</sub> hollow sphere multiscale structure exhibited a highly reversible capacity and excellent cycle stability, with an initial specific discharge capacity of up to  $1581 \text{ mAh g}^{-1}$  and a reversible capacity that was retained at  $542 \text{ mAh g}^{-1}$  after

300 cycles. These results were attributed to the unique structure of Ni-doped SnO<sub>2</sub> hollow spheres, which led to good electron transfer efficiency and structural stability. Furthermore, the nanostructure effectively reduced the Li-ion diffusion activation energy and band gap width and the hollow sphere structure was able to improve the comprehensive transmission efficiency and avoid the pulverization associated with volume changes. Therefore, this work provided new insights into the practical use of SnO<sub>2</sub> anode materials for Li-ion batteries.

## ACKNOWLEDGEMENTS

The authors gratefully acknowledge financial support from the National Nature Science Foundation of China (Grant Nos. 51801086).

## References

1. J.M. Tarascon and M. Armand, *Nature*, 414 (2001) 359-367.
2. P. Simon and Y. Gogotsi, *Nature Mater.*, 7 (2008) 845-854.
3. Y. Idota, T. Kubota, A. Matsufuji, Y. Maekawa and T. Miyasaka, *Science*, 276 (1997) 1395–1397.
4. X.W. Lou, Y. Wang, C. Yuan, J.Y. Lee and L.A. Archer, *Adv. Mater.*, 18 (2010) 2325-2329.
5. Y. Zhuo, S. Tymek, H. Sun, M.K.S. Barr, L. Santinacci and J. Bachmann, *Nanoscale Adv.*, 2 (2020) 1417-1426.
6. F. Zhang, C. Yang, X. Gao, S. Chen, Y. Hu, H. Guan, Y. Ma, J. Zhang, H. Zhou and L. Qi, *ACS Appl. Mater. Interfaces*, 9 (2017) 9620-9629.
7. H. Li, T. Yamaguchi, S. Matsumoto, H. Hoshikawa, T. Kumagai, N.L. Okamoto and T. Ichitsubo, *Nat. Commun.*, 11 (2020) 1584-1593.
8. Q. Tian, L. Li, J. Chen, L. Yang and S.I. Hirano, *J. Power Sources*, 376 (2018) 1-10.
9. S. Wang, X. Yu, J. Liu, P. Dong, Y. Zhang, C. Zhu, Z. Zhan and Y. Zhang, *J. Alloys Compd.*, 814 (2020) 152342-152350.
10. S.M. Jung, D.W. Kim and H. Y. Jung, *J. Mater. Chem. A*, 8 (2020) 8244-8254.
11. H. Kim, D.S. Yang, J.H. Um, M. Balasubramanian, J. Yoo, H. Kim, S.B. Park, J.M. Kim and W.S. Yoon, *J. Power Sources*, 413 (2019) 241-249.
12. M. Xie, X. Sun, S.M. George, C. Zhou, J. Lian and Y. Zhou, *ACS Appl. Mater. Interfaces*, 7 (2015) 27735-27742.
13. L. Yu, H. Hu, H.B. Wu and X.W.D. Lou, *Adv. Mater.*, 29 (2017) 1604563.
14. Y. Dong, S. Das, L. Zhu, T. Ben and S. Qiu, *J. Mater. Chem. A*, 4 (2016) 18822-18831.
15. L. Sun, H. Si, Y. Zhang, Y. Shi, K. Wang, J. Liu and Y. Zhang, *J. Power Sources*, 415 (2019) 126-135.
16. L. Zhang, M. Yang, S. Zhang, Z. Wu, A. Amini, Y. Zhang, D. Wang, S. Bao, Z. Lu, N. Wang and C. Cheng, *Sci. Rep.*, 6 (2016) 33597.
17. B. Cao, Z. Liu, C. Xu, J. Huang, H. Fang and Y. Chen, *J. Power Sources*, 414 (2019) 233-241.
18. H.M. Barkholtz, Y. Preger, S. Ivanov, J. Langendorf, L. Torres-Castro, J. Lamb, B. Chalamala and S.R. Ferreira, *J. Power Sources*, 435 (2019) 226777.
19. Q.A. Huang, Y. Li, K.C. Tsay, C. Sun, C. Yang, L. Zhang and J. Zhang, *J. Power Sources*, 400 (2018) 69-86.
20. B. Liu, X. Wang, H.S. Chen, S. Chen, H. Yang, J. Xu, H. Jiang and D.N. Fang, *J. Appl. Mech.*, 86 (2019) 041005.
21. Y.S. Lin, J.G. Duh and M.H. Hung, *J. Phys. Chem. C*, 114 (2010) 13136-13141.
22. J. Han, D. Kong, W. Lv, D.M. Tang, D. Han, C. Zhang, D. Liu, Z. Xiao, X. Zhang, J. Xiao, X. He, F.C. Hsia, C. Zhang, Y. Tao, D. Golberg, F. Kang, L. Zhi and Q.H. Yang, *Nat. Commun.*, 9 (2018)

402.

23. F.H. Aragon, J.A.H. Coaquirra, R. Cohen, L.C.C.M. Nagamine, P. Hidalgo, S.L.M. Brito and D. Gouvea, *Hyperfine Interact.*, 211 (2012) 77-82.
24. Y. Fan, Q. Kang, K. Zhang, J. Rong, J. Feng and X. Yu, *Ceram. Int.*, 46 (2020) 13615-1362.
25. X. Yu and Z. Zhan, *Nanoscale Res. Lett.*, 9 (2014) 516-521.
26. Q. Shao, H. Lin and M. Shao, *ACS Omega*, 5 (2020) 10297-10300.
27. Y.J. Wong, L. Zhu, W.S. Teo, Y.W. Tan, Y. Yang, C. Wang and H. Chen, *J. Am. Chem. Soc.*, 133 (2011) 11422-11425.
28. G. Kresse and J. Furthmüller, *Phys. Rev. B*, 54 (1996) 11169-11186.
29. G. Kresse and J. Furthmüller, Vienna Ab-initio Simulation Package (VASP), Vienna University, Vienna 2001.
30. P.E. Blochl, *Phys. Rev. B*, 50 (1994) 17953-17979.
31. J.P. Perdew, K. Burke and M. Ernzerhof, *Phys. Rev. Lett.*, 77 (1996) 3865-3868.
32. H.J. Monkhorst and J.D. Pack, *Phys. Rev. B*, 13 (1976) 5188-5192.
33. Z. Deng, J. Yan, F. Zhang, X. Wang, J.P. Xu and Z.Y. Zhang, *Acta Photonica Sinica*, 36 (2007) 110-115.
34. Z. Hu and X. Yu, *Mater. Res. Express.*, 6 (2019) 095089.
35. C.C. Yang and Q. Jiang, *Mater. Sci. Eng. B*, 131 (2006) 191-194.
36. W.H. Qi, M.P. Wang and Q.H. Liu, *J. Mater. Sci.*, 40 (2005) 2737-2739.
37. R. Kumar, G. Sharma and M. Kumar, *J. Thermodyn.*, 2013 (2013) 1-5.
38. Y.J. Hong, M.Y. Son and Y.C. Kang, *Adv. Mater.*, 25 (2013) 2279-2283.
39. X. Kou, N. Xie, F. Chen, T. Wang, L. Guo, C. Wang, Q. Wang, J. Ma, Y. Sun, H. Zhang and G. Lu, *Sens. Actuators B Chem.*, 256 (2018) 861-869.
40. P. Dou, Z. Cao, C. Wang, J. Zheng and X. Xu, *Chem. Eng. J.*, 320 (2017) 405-415.
41. Z. Yan, H. Sun, X. Chen, H. Liu, Y. Zhao, H. Li, W. Xie, F. Cheng and J. Chen, *Nat. Commun.*, 9 (2018) 2373.
42. W. Yao, S. Wu, L. Zhan and Y. Wang, *Chem. Eng. J.*, 361 (2019) 329-341.
43. Y. Zheng, T. Zhou, C. Zhang, J. Mao, H. Liu and Z. Guo, *Angew. Chem. Int. Ed.*, 55 (2016) 3408-3413.
44. Q. Tian, Y. Tian, W. Zhang, J. Huang, Z. Zhang and L. Yang, *J. Alloys Compd.*, 702 (2017) 99-105.
45. H. Xie, M. Chen and L. Wu, *Small*, 13 (2017) 1604283.
46. Z. Jiao, R. Gao, H. Tao, S. Yuan, L. Xu, S. Xia and H. Zhang, *J. Nanopart. Res.*, 18 (2016) 307.
47. Q. Han, F. Wang, Z. Wang, Z. Yi, Z. Na, X. Wang and L. Wang, *Ionics(Kiel)*, 24 (2017) 1049e1055.
48. X. Li, Z. Zhu, G.P. Nayaka, J. Duan, D. Wang, P. Dong, L. Huang, J. Zhao, S. Sun, X. Yu and Y. Zhang, *J. Alloys Compd.*, 752 (2018) 68-75.
49. Q. He, J. Liu, Z. Li, Q. Li, L. Xu, B. Zhang, J. Meng, Y. Wu and L. Mai, *Small*, 13 (2017) 1701504.
50. R. Liu, D. Li, C. Wang, N. Li, Q. Li, X. Lu, J.S. Spendelow and G. Wu, *Nano Energy*, 6.(2014) 73-81.
51. B. Zhang, C. Wang, Q. Ru, S. Hu, D. Sun, X. Song and J. Li, *J. Alloys Compd.*, 581 (2013) 1-5.
52. R. Liu, N. Li, G. Xia, D. Li, C. Wang, N. Xiao, D. Tian and G. Wu, *Mater. Lett.*, 93 (2013) 243-246.
53. Y. Lu, D. Zhang, Q. Zhang, Y. Huang, S. Luo, Y. Yao, S. Li and Q. Liu, *Biosens. Bioelectron.*, 79 (2016) 251-257.